

# PyCHAM (v1.0.0): a Python box model for simulating aerosol chambers

Simon P. O'Meara<sup>1,2</sup>, Shuxuan Xu<sup>1</sup>, David O. Topping<sup>1</sup>, M. Rami Alfarra<sup>1,2</sup>, Gerard Capes<sup>3</sup>, Douglas Lowe<sup>3</sup>, and Gordon McFiggans<sup>1</sup>

<sup>1</sup>Department for Earth and Environmental Sciences, University of Manchester, UK, M13 9PL

<sup>2</sup>National Centre for Atmospheric Science

<sup>3</sup>Research Computing Services, University of Manchester, UK, M13 9PL

**Correspondence:** Gordon McFiggans (g.mcfiggans@manchester.ac.uk)

**Abstract.** Box models of aerosol chambers simulate multi-phase processes to reproduce chamber observations. Comparison of chamber measurements with model estimates allows improvement of process understanding that can be transferred to ambient atmosphere simulations, thereby enabling evaluation of how chamber insights impact the real-world atmosphere. However, there is not yet an open-source modelling software designed for ease of use for chamber scientists. To fulfil this requirement

5 PyCHAM (CHemistry with Aerosol Microphysics in Python) has been produced and is described and verified here. PyCHAM allows acceleration of knowledge transfer from chamber measurements to regional and global simulations involving aerosol. In this model description paper we present governing equations, verification, and assessment of sensitivities to model parameters. The PyCHAM software is built for desktop computers, with releases available at <https://github.com/simonom/PyCHAM>.

*Copyright statement.* TEXT

## 10 1 Introduction

For the mixture of gases and particles (aerosol) that comprise atmospheres our paucity of understanding presents serious societal issues. Forecasts of climate change and air quality underpin international and national legislation (e.g. UNFCCC, 2018; UK Government, 2020; European Commission Environment, 2020) that demands major economic and political restructuring (MIT Science and Policy of Global Change, 2020) in addition to driving ethical incentives to change behaviour. Whilst our

15 understanding is sufficient to target emission decreases for certain pollutants, uncertainty around the extent of decrease and type of emission remains considerable (Heal et al., 2012; Johnson et al., 2018; Tong et al., 2019). To improve the efficiency of emission targets requires improved understanding of the gas- and condensed-phase processes determining atmospheric abundance of trace constituents. This is the aim of aerosol chambers, which have the advantage of controlling physicochemical conditions to isolate and observe select processes (Schwantes et al., 2017; Charan et al., 2019).

20 Many major advances in atmospheric modeling have arisen from chamber observations, for example, the partitioning of vapours to particles developed in Odum et al. (1996) and applied in Meng et al. (e.g. 1997) and the gas-phase chemistry

of ozone as part of the Master Chemical Mechanism (MCM) developed in Jenkin et al. (1997) and applied in Ying and Li (e.g. 2011). Such advances can be incorporated into improved chamber models (e.g. Charan et al., 2019), aiding the design of experiments to interrogate further processes and systems (e.g. Riva et al., 2020). As chamber use has multiplied, so too have chamber models, with many now published (Naumann, 2003; Pierce et al., 2008; Lowe et al., 2009; Roldin et al., 2014; Sunol et al., 2018; Topping et al., 2018; Charan et al., 2019; Roldin et al., 2019). To our knowledge, however, these have not prioritised accessibility and/or usability. Consequently, chamber research groups without access or ready application of a model are limited in the design, interpretation and advancement of both chamber experiments and their contribution to models. To address this limitation, the EUROCHAMP2020 (Oliveri, 2018) research project and National Centre for Atmospheric Science have developed PyCHAM (CHemistry with Aerosol Microphysics in Python), a zero-dimensional aerosol chamber box model. The model software along with the figures (and required inputs) from this paper are available open-source here: <https://github.com/simonom/PyCHAM>.

In this paper the processes represented in PyCHAM are described, along with details of software application. Where relevant, equations are presented and output from PyCHAM verified. In the following two sections the objectives, rationale and structure of the software are explained.

## 2 Purpose and Scientific Basis

Consistent with the criteria set by the EUROCHAMP2020 research project (Oliveri, 2018), PyCHAM is open source, user-friendly and representative of the latest scientific understanding. Python is the chosen language for two key reasons: code can be transferred between computers without the limitation of requiring a certain compiler (thereby improving ease of use), and the relatively versatile parsing capability which allows the user to readily vary model inputs. Inside the README manual of the software's home folder are installation and setup instructions that have been verified by reviewers (O'Meara et al., 2020). Application of the software on a desktop computer, including input descriptions and specifications, is detailed in the manual and described more generally below.

Aerosol chambers (interchangeably called smog chambers), defined as those used for interrogating gas- and particle-phase processes, provide a method for isolating specific processes of interest without the convoluting effects present in the ambient atmosphere. Ultimately the goal of the chamber is to improve understanding and quantitative constraint on the evolution of the physicochemical properties of the gas- and particle-phase (Schwantes et al., 2017; Charan et al., 2019; Hidy, 2019). The aim of EUROCHAMP2020 was to advance application of chambers by tackling various weaknesses; consequently, the publications (Oliveri, 2018) resulting from the project provide a thorough introduction to chamber capabilities and operations. A chamber experiment begins with a container (walls are made of a range of materials, but frequently of fluorinated ethylene-propene film (FEP Teflon)), followed by one of two approaches to inlet components: batch mode whereby set volumes of gas or particle are injected at specific times, or in flow mode with a constant influx of gas or particle (Jaoui et al., 2014). The model variables input file for PyCHAM allows users to setup simulations for both modes along with several other specifications representing the majority of aerosol chamber experiments: with or without seed particles (for absence of seed particles nucleation can be

55 simulated); variable temperature, pressure and relative humidity; for lit experiments, either natural light intensity (for open roof chambers) or known actinic flux (for chambers with bulbs) that can be turned on and off at set times. A full list of the model variables is given in the user manual.

Two previous models act as platforms on which PyCHAM developed: the Microphysical Aerosol Numerical model Incorporating Chemistry (MANIC) (Lowe et al., 2009) and PyBox (Topping et al., 2018), with the former guiding multi-phase  
60 processes and the latter guiding python parsing and automatic generation of chemical reaction modules. With the combination of these two pillars, PyCHAM provides a very flexible tool for aerosol chamber scientists whilst representing the latest understanding of key chamber processes: gas-phase photochemistry, gas-particle and gas-wall partitioning, coagulation, nucleation and particle deposition to walls. Consequently its full list of applications is numerous and will certainly grow as chamber experiments evolve, however, key examples include designing chamber experiments, testing and developing gas-phase chemistry  
65 mechanisms, quantifying particle and wall partitioning parameters, testing and developing nucleation models and interrogating the effects of processes on secondary organic aerosol (SOA) evolution.

The processes included in PyCHAM may also be represented in large-scale (regional and global) atmospheric models and it is intended that once a process has been successfully modelled by PyCHAM it can be transferred, possibly via parameterisation, to a large-scale model for evaluation, similar to the modelling advances mentioned in the introduction. For rigorous elucidation  
70 of a given process, it is necessary that convoluting processes have been verified and evaluated. This paper presents verification (through comparison with established models) that the individual process models in the base version of PyCHAM are accurate. It is the responsibility of the user to ascertain that experiments and associated modelling do not compromise the investigation of a given process through uncertainties of a convoluting process. This is challenging as multiple processes can be coupled inside a chamber experiment. However, PyCHAM is designed to realistically model this coupling through simultaneous integration  
75 of gas-phase photochemistry, gas-particle partitioning and gas-wall partitioning.

To illustrate the use of PyCHAM, a simulation has been designed around the role of nitrate radical ( $\text{NO}_3$ ) oxidation of limonene in SOA evolution. Such experiments have important implications for indoor air quality, particularly at night time when the photolysis of  $\text{NO}_3$  ceases (Waring and Wells, 2015), therefore lights were turned off for this simulation. Accurate results can constrain the exposure of individuals to harmful aerosol (Carslaw and Shaw, 2019). Following a similar approach  
80 to the experiment of Fry et al. (2011), the effect of  $\text{NO}_3$  in the presence of ozone ( $\text{O}_3$ ) can be replicated through introduction of  $\text{O}_3$  and nitrogen dioxide ( $\text{NO}_2$ ) into the chamber whilst removing the effect of the hydroxyl radical ( $\text{OH}$ ) through addition of excess carbon monoxide. At sufficient concentrations, this mixture causes particle nucleation (Fry et al., 2011), which we simulate here through the nucleation parameterisation described below.  $\text{O}_3$ ,  $\text{NO}_2$  and limonene are injected again later but with the addition of seed aerosol for reproduction of indoor environments with substantial existing particulate matter.

85 Simulation results in Fig. 1 show the time-profile of gas-phase concentrations of reactant components and mass concentrations of grouped components in the particle and wall phase. The contribution of  $\text{NO}_3$  oxidation of limonene to SOA is indicated by the particle organic nitrate curve. The particle inorganic nitrate curve represents the contribution of dinitrogen pentoxide ( $\text{N}_2\text{O}_5$ ) and nitric acid ( $\text{HNO}_3$ ) to the particle phase. Here we simulate the hydrolysis of  $\text{N}_2\text{O}_5$  into the aqueous phase of particles and wall by setting its activity coefficient to zero and its accommodation coefficient according to Lowe et al. (2015).

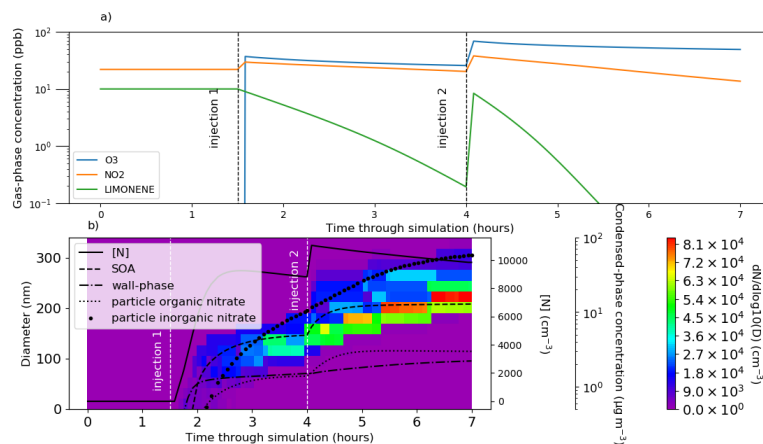


**Figure 1.** Limonene oxidation in the dark with and without seed particles. In a), the gas-phase concentrations of key components and in b), the particle properties. At the start 10 ppb limonene, 22 ppb NO<sub>2</sub> and 500 ppm CO are introduced. At 1.5 hours 38 ppb O<sub>3</sub> and 8 ppb NO<sub>2</sub> are injected (injection 1). At 4 hours a further injection of O<sub>3</sub> (45 ppb), limonene (10 ppb) and NO<sub>2</sub> (19.0) is coincident with an injection of seed aerosol ( $10 \mu\text{g m}^{-3}$  with a mean diameter of  $0.2 \mu\text{m}$ ) (injection 2). In b), the total particle number concentration ([N]) corresponds to the first of the right axes, mass concentrations of: secondary organic aerosol mass concentration (SOA), components condensed to walls (wall-phase) and sum of particle-phase organic components with a nitrate functional group (particle organic nitrate) correspond to the second of the right axes, whilst number size concentrations correspond to the filled contours, colour bar and left axis. Whilst [N] includes seed particles, SOA excludes the seed material and all mass concentrations exclude water.

As detailed below, for accurate application of PyCHAM output the partitioning of components to chamber walls is key; without its correct reproduction, comparison against measurements is compromised. However, with correct wall process constraint, simulations such as Fig. 1 can be compared against measurements to verify process understanding. For example, gas-phase organic chemistry research has recently revealed the role of highly oxidised molecules (HOM) (Ehn et al., 2014), with the Peroxy Radical Autoxidation Mechanism (PRAM) simulating their chemistry (Roldin et al., 2019). For the results in Fig. 1, the PRAM scheme has been coupled with that of the Master Chemical Mechanism (MCM) (Jenkin et al., 1997; Saunders et al., 2003). Whilst we do not yet have the measurement ability to quantify the particle- or gas-phase concentrations of individual HOM components, comparison of particulate loading in experiments where HOM is detected provides a useful evaluation tool.

### 3 General Structure

For ease of navigation, PyCHAM has a modular structure with each key physicochemical process assigned an individual module. At the core of PyCHAM lies simultaneous numerical integration of three coupled processes: gas-phase photochemistry, vapour-particle partitioning and vapour-wall partitioning. The ordinary differential equations (ODEs) for these processes are solved by the backward differentiation formula (which has proven reliability (Jacobson, 2005)) from the CVODE Sundials

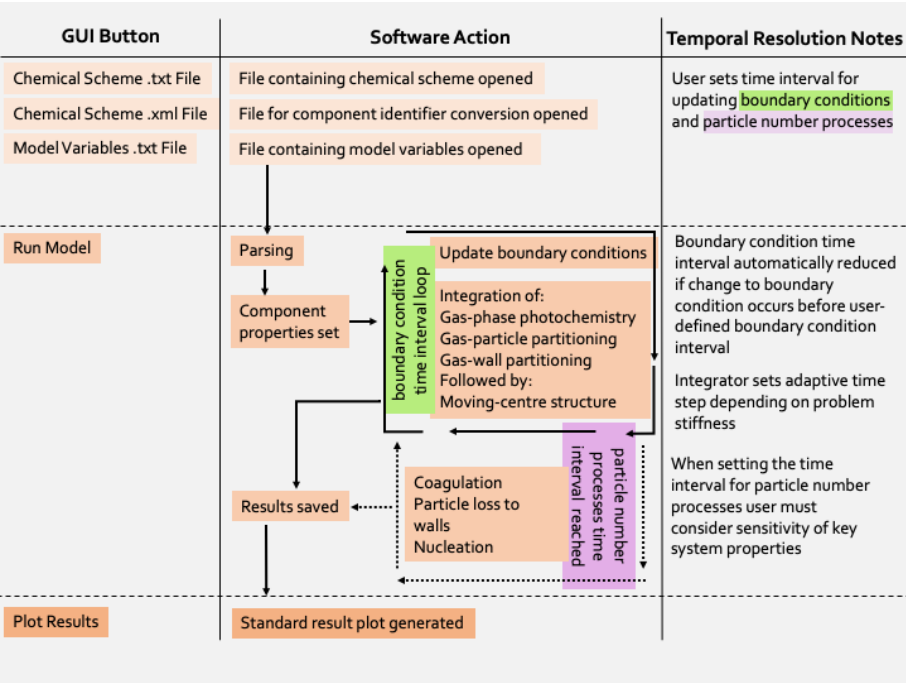


**Figure 2.** Schematic outlining the steps in the PyCHAM model, as directed by the GUI buttons, with arrows showing the sequence of code. The repeat of model loop time intervals terminates when the end time is reached. The dashed lines indicate the conditional action of modelling the processes affecting particle number (determined by the particle number process time interval).

software (Hindmarsh et al., 2005). We use a python wrapper for sundials called Assimulo (Andersson et al., 2015), allowing communication between the solver and the Python code. The model structure is outlined in the schematic of Fig. 2, where we introduce the time interval for updating boundary conditions, such as whether seed particles injected. The boundary condition time interval is passed to the integrator, which adaptively sets sub-time steps depending on problem stiffness. Because coagulation, particle loss to walls and nucleation, which all affect particle number concentration, are generally slower than chemical reactions and partitioning, they are operator split. Therefore users also set a time interval for these particle number processes to be solved (Fig. 2). The sensitivity of system properties to the operator split is illustrated in Section 11.

In the example model output of Fig. 1 several features of PyCHAM are demonstrated. First, the coupling of gas-phase chemistry and resulting partitioning of vapours with sufficiently low volatility to particles and walls. Nucleation has been simulated prior to the introduction of seed particles with approximate values given for the tuned nucleation parameters described below such that nucleation begins at the introduction of ozone, has a duration of thirty minutes and produces a peak number concentration similar to that of the seed particle. Finally, coagulation and particle wall loss (the latter using the model of McMurry and Rader (1985)), contribute to the decay in particle number concentration.

The PyCHAM software is initiated with the terminal/command window to generate a graphical user interface (GUI). Via the GUI, users select three files (Fig. 2) representing: i) the chemical scheme, ii) a file associating the chemical identifiers inside

the chemical scheme to their Simplified Molecular Input Line Entry System (SMILE) strings (Weininger, 1988), and iii) a model variables file. A fourth button on the GUI starts the simulation. Unit tests to ensure individual modules operate correctly  
120 are contained in the software package.

A parsing module interprets the chemical scheme and uses the chemical identifier conversion file to match component identifiers to their SMILE strings. Additionally, modules are automatically created that will calculate time-dependent chemical reaction rates and track the rate of change of specified components. A gas-phase initiation module sets the starting concentrations of injected components, whilst a particle-phase initiation module establishes any seed particles at experiment start. The  
125 integration module is then called, which loops over the boundary condition time interval to update boundary conditions and solve the ODEs for gas-phase photochemistry and partitioning (Fig. 2). Following integration, the moving-centre module is called to redistribute particles that have changed size sufficiently to cross size bin boundaries. The operator-split processes of particle loss to wall, coagulation and nucleation are the final calculations of a time step if their time interval is met. A saving module stores results for gas, particle and wall concentrations, corresponding time, particle number size distributions (with and  
130 without water) and constants such as component molecular weight.

The fifth and final button on the GUI will display and save graphs of the temporal profiles of number size distribution, secondary aerosol mass concentration, total particle number concentration, and the gas-phase concentrations of specified components. The programme can be stopped via the terminal when in integration mode, or outside this mode it can be terminated by closing the GUI.

135 Below we describe and verify the processes described above as coded in PyCHAM. Necessarily each process is treated in isolation, however, Fig. 1 and its associated text exemplify the coupling of mechanisms for a real world application.

## 4 Component Properties

The components included in the user-defined chemical scheme are automatically allocated three properties by the PyCHAM software: molecular weight, liquid density and liquid saturation vapour pressure. Molecular weights are estimated by passing  
140 SMILE strings to the pybel module of the Open Babel chemical toolbox (O’Boyle et al., 2011). pybel is installed as part of the PyCHAM package and generates unique chemical identifiers for each component based on their SMILE string. For estimating component densities and liquid-phase saturation vapour pressures, the pybel chemical identifiers are passed to the UManSysProp module (Topping et al., 2016) which is updated on the first run of PyCHAM and at the request of the user (via the model variables file) thereafter (requires internet connection). By default the UManSysProp module applies the liquid  
145 density estimation method of Girolami (1994) (recommended by Barley et al. (2013)) and the liquid saturation vapour pressure estimation method of Nannoolal et al. (2008) (recommended by O’Meara et al. (2014)). Component vapour pressures have a first order effect on partitioning between phases, however estimates for certain components, particularly those with relatively low vapour pressures as these are most difficult to measure experimentally and therefore inform estimation methods, are associated with considerable uncertainty (O’Meara et al., 2014). Consequently, users can also specify the vapour pressures of

certain components. Similarly, although the default particle- and wall-phase activity coefficient for all components is one, users may set an alternative value for specific components in the model variables folder.

## 5 Gas-phase Chemistry

For a chamber experiment including injection of reactive components, chemical reactions in the gas-phase drive the disequilibria that changes all three phases: gas, particle and wall. As mentioned above, the MCM provides a near-explicit model of gas-phase chemistry for several organic precursors, and developments such as PRAM include updates to our understanding. PyCHAM is designed to accommodate such chemical schemes whilst also accepting very simplified or even empty chemical equation files. Whilst the software manual details the requirements for input chemical schemes and chemical identifier conversion files, here we describe how PyCHAM deals with chemistry. Equations of the general form:

$$s_{r_1}r_1 + s_{r_2}r_2 \dots = s_{p_1}p_1 + s_{p_2}p_2 \dots \quad (1)$$

where  $s$  represents stoichiometric number,  $r$  reactants and  $p$  products, are expressed as the ODEs:

$$\frac{d[r_i]}{dt} = -s_{r_i}k_r\Pi_{j=1}^{j=n}([r_j]^{s_{r_j}}) \quad (2)$$

$$\frac{d[p_i]}{dt} = s_{p_i}k_r\Pi_{j=1}^{j=n}([r_j]^{s_{r_j}}) \quad (3)$$

where  $n$  is the total number of reactants and  $r_j$  is a given reactant for a given reaction.  $k_r$  is the reaction rate coefficient.

Users must therefore provide a reaction(s) of the form in Eq. 1 and an associated reaction rate coefficient inside a chemical scheme file. Naming of chemical components inside the chemical scheme is unrestricted, however, the software must be able to convert names to SMILES (Weininger, 1988). Therefore, users must provide a separate file stating a unique SMILES string for every component (Fig. 2).

Inside the parsing module, reaction rate coefficients, reactant and product identities and their stoichiometric numbers are established from the chemical scheme file. To separate these properties either default formatting may be used, or a variant, so long as the appropriate changes are made inside the model variables file. By default, MCM kinetic pre-processor formatting is used (Jenkin et al., 1997; Saunders et al., 2003). The MCM is presented via a user-friendly website (Rickard and Young, 2020), it is recommended as a state-of-the-science resource for acquiring atmospheric chemistry schemes.

Reaction rate coefficients can be functions of temperature, relative humidity, pressure (set by user in model variables file) and concentrations of: third body, nitrogen, oxygen and peroxy radicals. Third body, nitrogen and oxygen concentrations are calculated by the ideal gas law with the user-set temperature and pressure. As in the MCM, the chemical scheme file can include generic reaction rate coefficients (those that have an identifier which is used as the reaction rate coefficient for one or more reactions). Furthermore, the scheme can include a list of peroxy radicals, which is necessary if reaction rate coefficients are to be functions of radical concentrations.

Photochemistry is controlled through stating light on/off times inside the model variables file. The treatment of photochem-  
 180 istry is determined by the user and depends on the chemical scheme employed. In the case of the MCM scheme and natural  
 sunlight, the scattering model based on Hayman (1997) and described in Saunders et al. (2003) is invoked by stating the rel-  
 evant spatial and temporal coordinates in the model variables file. For artificial lights, users must provide a file stating the  
 wavelength-dependent actinic flux (as described in the manual). The model then calls on either the absorption cross-section  
 and quantum yield estimates of MCM v3.3.1 or of a user-defined file.

185 Users can also specify the components they wish to be tracked during a simulation. PyCHAM automatically generates a  
 module that calculates and records the rate of change of the gas-phase concentration of the given component as a function  
 of individual gas-phase reactions and partitioning. This function is essential for ensuring individual processes affecting a  
 component are being accurately modelled and for trouble-shooting.

## 5.1 Verification

190 To verify the photochemistry section of PyCHAM, gas-particle partitioning and gas-wall partitioning were turned off, leaving  
 only gas-phase chemistry to be solved. Here we compare against AtChem2 (Sommariva et al., 2018) as a model benchmark,  
 with both using MCM chemical schemes. Fig. 3 shows the deviation with experiment time for two standard aerosol chamber  
 characterisation experiments:  $\alpha$ -pinene ozonolysis in the presence (plot a) and absence (plot b) of NO<sub>x</sub>. To test both the dark  
 and lit scenarios, the simulation is for an environmental chamber with an open roof, starting at midnight and finishing at  
 195 midday. Initial concentrations of  $\alpha$ -pinene and O<sub>3</sub> were equal at 21.1 ppb for both experiments, whilst for NO<sub>x</sub> the initial  
 concentration was 9.8 ppb in Fig. 3a and 0 ppb in Fig. 3b. Latitude was set to 51.51, longitude to 0.13 (London, UK) and the  
 date to 1<sup>st</sup> July. Deviation was calculated using:

$$\sigma_{i,t} = \left( \frac{s_{i,t} - b_{i,t}}{\vee(b_i)} \right) 100, \quad (4)$$

where  $\sigma_{i,t}$  is the percentage deviation for component  $i$  at time  $t$ ,  $s$  is the PyCHAM result,  $b$  is the AtChem2 result and  $\vee(b_i)$   
 200 is the AtChem2 maximum for a given component during the simulation.

Whilst Fig. 3 indicates that PyCHAM performs well for components with both relatively short (e.g. OH) and long (e.g.  
 $\alpha$ -pinene) lifetimes, it is necessary to ascertain that agreement is gained through the correct mechanism. Users of PyCHAM  
 and AtChem2 can specify components that have rates of change tracked. In Fig. 4 we use this to compare the reaction rates for  
 formaldehyde for the same  $\alpha$ -pinene ozonolysis simulations used for Fig. 3. The deviations were again calculated using Eq. 4,  
 205 but with concentrations replaced by gas-phase concentration rate of change due to a given reaction. Of the loss and production  
 reactions for formaldehyde the two of each with greatest deviation are shown in Fig. 4. The low deviation values in Fig. 4  
 demonstrate that PyCHAM indeed integrates gas-phase photochemistry correctly.



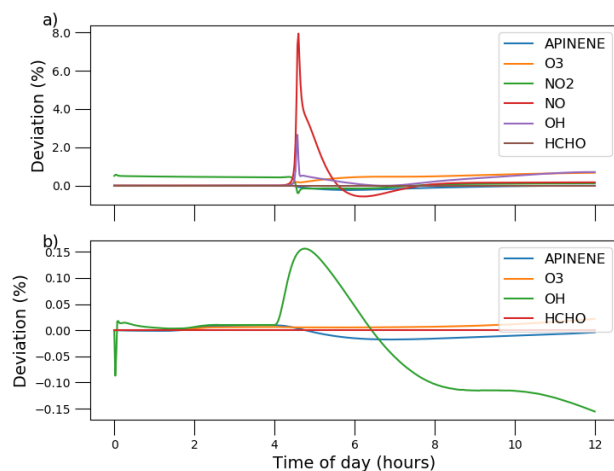


**Figure 3.** Gas-phase photochemistry verified; simulations of photochemistry in an aerosol chamber exposed to natural light, where deviation is defined in Eq. 4.  $\alpha$ -pinene ozonolysis is simulated in both plots, with  $\alpha$ -pinene and O3 given the same initial concentrations of 21.1 ppb, and initial NO<sub>x</sub> concentration in a) 9.8 ppb and in b) 0 ppb. For both simulations, the environmental chamber is transparent and exposed to daylight without cloud interference, with dawn at approximately 4:00 hours. The particle-phase and vapour losses to walls are turned off in PyCHAM to be consistent with the AtChem2 model.

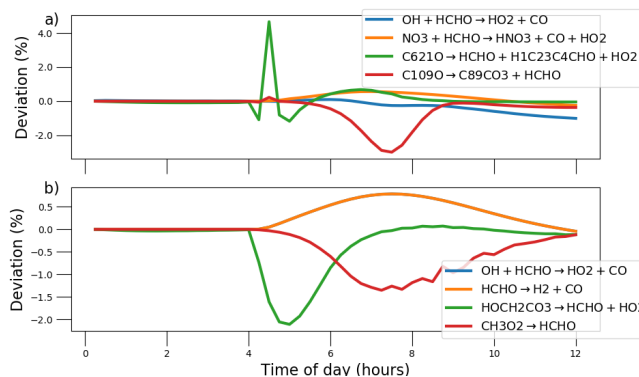


**Figure 4.** Deviation of PyCHAM simulated rate of change of formaldehyde (HCHO) from AtChem2 simulations for the MCM reactions given in the legends. Where the definition for deviation is given by Eq. 4. Both plots are results for the  $\alpha$ -pinene ozonolysis reaction described in the main text for Fig. 3, with a) in the presence of NO<sub>x</sub> and b) in the absence of NO<sub>x</sub>.

## 5.2 Photochemical Sensitivity to Temporal Resolution

For minimising the time required for simulation, users can increase the boundary condition time interval (Fig. 2). For dis-  
 210 continuous changes to the simulation, such as short injections of components, PyCHAM automatically adapts the boundary

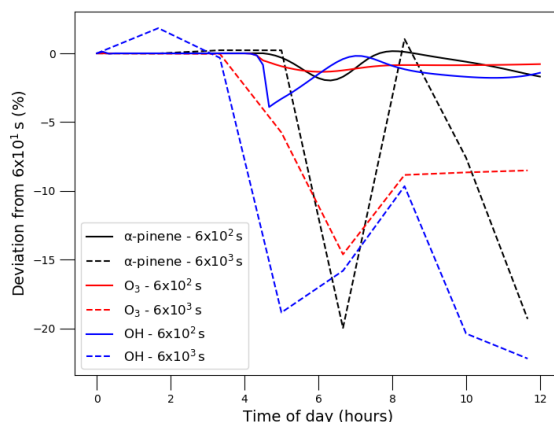


**Figure 5.** Illustrating the effect of boundary condition time interval resolution in PyCHAM on gas-phase concentrations of  $\alpha$ -pinene, O<sub>3</sub> and OH for the  $\alpha$ -pinene ozonolysis in presence of NO<sub>x</sub> experiment described above for Fig. 3. Time intervals were set to  $6 \times 10^2$  and  $6 \times 10^3$  s as shown in the legend, and the deviation is that from results for a time interval of  $6 \times 10^1$  s.

condition time interval to coincide with the change. However, for continually changing conditions such as continuous injection of components or changing natural light intensity, the boundary condition time interval is determined by the user input. Therefore, increases in time interval leads to loss of temporal detail. The user must balance the need for reduced time for simulation against loss of accuracy in simulated gas-phase concentrations. To illustrate the issue, the same scenario described above for Fig. 3 is used, with Fig. 5 showing the effect on estimated gas-phase concentrations of increasing the boundary condition time interval by an order of magnitude from  $6 \times 10^1$  to  $6 \times 10^2$  and  $6 \times 10^3$  s. Deviation was calculated by replacing AtChem2 inputs to Eq. 4 with simulated results from PyCHAM at a 60 s resolution. Simulation time for the  $6 \times 10^3$  s resolution was 52 s using a 2.5 GHz Intel Core i5 processor, with factor increases of 7 and 53 for  $6 \times 10^2$  and  $6 \times 10^3$  s resolutions, respectively. Users are advised to conduct a similar test if their chemical scheme or environmental conditions vary significantly from those here.

## 220 6 Gas-wall partitioning

The partitioning of gases to the chamber wall is often termed wall loss as the net movement is from the gas phase to the wall (for an initially clean chamber wall). Traditionally this process has been viewed as an inconvenience since chamber results often depend on the concentration of gas- and particle-phases of certain components, whilst the fraction of these components lost to walls is poorly constrained. Several studies have focussed on partitioning to Teflon walls, which are frequently employed (Matsunaga and Ziemann, 2010; Zhang et al., 2015; Zhao et al., 2018), however, the process remains poorly modelled across the wide range of chamber materials, relative humidities, gas-phase loading, component volatilities and activity coefficients present in chamber experiments (e.g. Day et al., 2017; Stefenelli et al., 2018). It is therefore preferable to allow the user to fit vapour losses to walls through the tuning of two wall loss parameters, one primarily determining equilibrium, called the

effective wall mass concentration ( $C_w$ ), and one determining rate of partitioning, the mass transfer coefficient ( $k_w$ ). These  
 230 influence gas-wall partitioning through an equation of the same framework as gas-particle partitioning (which is described  
 below and in Zaveri et al. (2008)):

$$\frac{dC_{i,g}}{dt} = -k_w \left( C_{i,g} - \frac{C_{i,w}}{C_w} p_i^0 \gamma_i \right), \quad (5)$$

$$\frac{dC_{i,w}}{dt} = k_w \left( C_{i,g} - \frac{C_{i,w}}{C_w} p_i^0 \gamma_i \right), \quad (6)$$

where  $p_i^0$  is the liquid (sub-cooled if necessary) saturation vapour pressure of component  $i$  and  $\gamma_i$  is its activity coefficient on  
 235 the wall. Following the conclusions of Matsunaga and Ziemann (2010) and Zhang et al. (2015),  $k_w$  represents factors such as  
 gas- and wall-phase diffusion, turbulence, accommodation coefficient and the chamber surface area to volume ratio, whilst  $C_w$   
 reflects the adsorbing and/or absorbing properties of the wall, including effects of relative humidity, surface area, diffusivity and  
 porosity. We recommend the iterative fitting of  $k_w$  and  $C_w$  to observations through minimising observation-model residuals.  
 $C_w$  in PyCHAM is independent of condensates to the wall, which is consistent with the findings of Matsunaga and Ziemann  
 240 (2010) and Zhang et al. (2015).

A major distinction between the gas partitioning to particles and walls is the much greater size of the wall, where size is  
 represented by surface area or volume depending on whether adsorption or absorption is the main partitioning mechanism,  
 respectively. It could be argued that the effective wall mass concentration is massive compared to the concentration of wall-  
 phase components, making the Raoult (mole fraction, ( $\frac{C_{i,w}}{C_w}$ )) term in Eq. 5 redundant. Following this argument, the gas-wall  
 245 partitioning equation becomes:

$$\frac{dC_{i,g}}{dt} = -k_w \left( C_{i,g} - \frac{p_i^0 \gamma_i}{C_w} \right). \quad (7)$$

However, this approach is unphysical as it removes the dynamic property of partitioning, instead, the  $\frac{p_i^0 \gamma_i}{C_w}$  term implies a  
 fixed concentration of wall-phase component in the gas-phase just above the wall and introduces several issues. First, it implies  
 that components with higher volatility and activity coefficient have a greater concentration on the wall, which is unrealistic.  
 250 Second, the fixed wall concentration allows for loss of mass conservation for components with  $C_{i,g} < \frac{p_i^0 \gamma_i}{C_w}$  since components  
 may evaporate from the wall despite having no presence there. Conversely, components with  $C_{i,g} > \frac{p_i^0 \gamma_i}{C_w}$  may undergo an  
 unrealistic degree of condensation to the wall because the evaporation of their wall-phase is unaccounted for.

## 6.1 Tuning gas-wall partitioning parameters

Next we illustrate the sensitivity to  $k_w$  and  $C_w$  in Eq. 5. The same simulation setup described above for Fig. 3 was used  
 255 though with  $\alpha$ -pinene replaced by isoprene with a concentration at experiment start of 63.4 ppb. Seed particles comprised  
 of ammonium sulphate with mean diameter 0.5  $\mu\text{m}$  and number concentration  $6 \times 10^2 \text{ cm}^{-3}$  were introduced at experiment  
 start. Pure component liquid saturation vapour pressures were estimated by the Nannoolal et al. (2008) method and activity

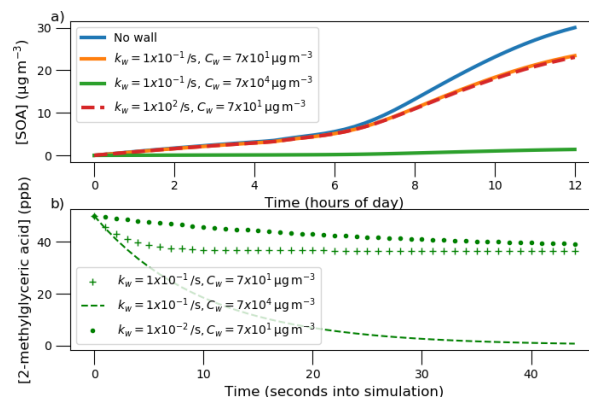


**Figure 6.** In a) sensitivity of SOA mass concentration on the gas-wall partitioning parameters  $k_w$  and  $C_w$  from Eq. 5. Seed particles with a concentration of approximately  $70 \mu\text{g m}^{-3}$  were present at the start of the experiment. Initial concentrations of ozone, isoprene and NO<sub>2</sub> were set to 21.1, 63.4 and 9.8 ppb, respectively. With regards to photolysis rates, the simulation made the same considerations as in Fig. 3, where natural sunlight drove reactions after dawn at approximately 4:00 am. In b), the same sensitivity is assessed, but for a control experiment where only a single organic component is present.

coefficients for all components were assumed one. To begin, both  $k_w$  and  $C_w$  were set sufficiently low to effectively turn off gas-wall partitioning. Second,  $C_w$  was set equal to the mass concentration of seed particle ( $70 \mu\text{g m}^{-3}$ ) and  $k_w$  raised to  $1 \times 10^{-1} \text{ s}^{-1}$  at which a notable decrease in [SOA] was observed. Third,  $k_w$  was held whilst  $C_w$  was raised three orders of magnitude greater than the seed mass concentration. Fourth,  $C_w$  was held at  $70 \mu\text{g m}^{-3}$  and  $k_w$  was raised by three orders of magnitude. The effect on SOA mass concentration is given in Fig. 6 and demonstrates that at sufficiently large values of  $C_w$ , SOA production can be effectively suppressed through competitive uptake of vapours to chamber walls. However, for a given  $C_w$ , there is a limit on suppression of SOA formation due to  $k_w$  increase as it affects only the rate of partitioning with walls rather than the condensable fraction.

To guide constraint for wall loss parameters, we follow the example of Matsunaga and Ziemann (2010), with a control experiment comprising a single semi-volatile component introduced to the chamber at the start of the simulation at 50 ppb. We chose 2-methylglyceric acid which has an estimated particle mass concentration saturation vapour pressure ( $C^*$ ) of  $1.15 \times 10^2 \mu\text{g m}^{-3}$  at 298.15 K (the simulation temperature) and is an observed oxidation product of isoprene (Surratt et al., 2006). No other components or particles are introduced. With regards to designing a control experiment for tuning  $C_w$  and  $k_w$ , the results shown in Fig. 6b demonstrate that a component with a  $C^*$  close to the  $C_w$  has large sensitivity to the  $C_w$  value, thereby allowing greatest ease of tuning. Note, that this sensitivity can be altered through varying chamber temperature (and therefore the  $C^*$  of a component), or through varying component. Furthermore, to discern the effect of  $k_w$  a component with substantial partitioning to walls is required. When quantifying  $k_w$  it is worthwhile considering the required precision, because as Fig. 6a demonstrates, above a certain value, no further effect on SOA concentration results.

## 7 Gas-particle partitioning and sectional approach

PyCHAM simulations, like chamber experiments, are possible with and without seed particles. For seed particle experiments, the user defines number size distribution and composition inside the model variables input file. Furthermore, because PyCHAM uses size bins to discretise particles, users can state the number of size bins, lower and upper bin bounds and whether they would like the bins to be spread linearly or logarithmically in radius space.

Particles can grow or shrink as a direct consequence of three processes modelled by PyCHAM: gas-particle partitioning, coagulation and nucleation. Whilst coagulation and nucleation are discussed below, readers are referred to Zaveri et al. (2008) for a thorough explanation of gas-particle partitioning. The transition regime correction factor required for the partitioning estimation in PyCHAM is from Fuchs and Sutugin (1971). Furthermore, the unit test `test_kimt_calc` is available to check that the Kelvin and Raoult effects of the PyCHAM partitioning equation are accurate (e.g. through comparison with Fig. 16.1 of Jacobson (2005)).

In this section we focus on redistribution of particles between size bins following a change in size due predominately to gas-particle partitioning. PyCHAM does this using the moving-centre structure (Jacobson, 2005). The moving-centre approach has the advantage of minimal numerical diffusion, however, it suffers from loss of particle history due to its combining of mass of particles originally from varying size bins (Zhang et al., 1999). The user must consider this weakness when determining whether the model is suitable for their purpose. To maintain stability in numerical solutions and improve model accuracy, a condition inside the moving-centre module of PyCHAM iteratively reduces the boundary condition time interval if particles in a size bin change volume sufficiently to be allocated to a size bin beyond the adjacent one, or if particles have an unrealistic negative volume (possibly due to evaporation).

Here we assess the moving-centre method through analysis of output during two relatively intense (and therefore testing) periods of gas-particle partitioning and compare to benchmark simulations. The simulations also illustrate two further means of component influx to chambers using PyCHAM in addition to the simulations above where components were introduced with an initial pulse. In the first case a constant flux of sulphuric acid is added to a chamber with seed aerosol typical of hazy conditions following the benchmark simulation of Zhang et al. (1999). For consistency with the benchmark, gas and particle partitioning to walls was turned off and sulphuric acid was assumed to be non-volatile. The analysis section of Zhang et al. (1999) notes that to resolve the growth of smallest particles in this scenario, spatial resolution must be at least 100 size bins, therefore we use this value and set the solution time interval to 90 s for a total 12 hour simulation.

The exact solution to this condensational growth problem is given in Fig. 7a) (taken from Fig. 3 of Zhang et al. (1999)) and is provided by the full-moving structure. When PyCHAM is compared against the exact solution, the tri-modal distribution is present with mean values at the correct particle size though with some disagreement in the peak height and spread. The degree of agreement is significantly better than for the 13 size bin moving-centre simulation presented in Zhang et al. (1999) and indicates that PyCHAM is operating as intended. Our results in Fig. 7a are a two-point moving average which is often necessary for the moving-centre structure because its requirement that all particles in a size bin be transferred to the adjacent bin means that some bins will intermittently have zero particles.

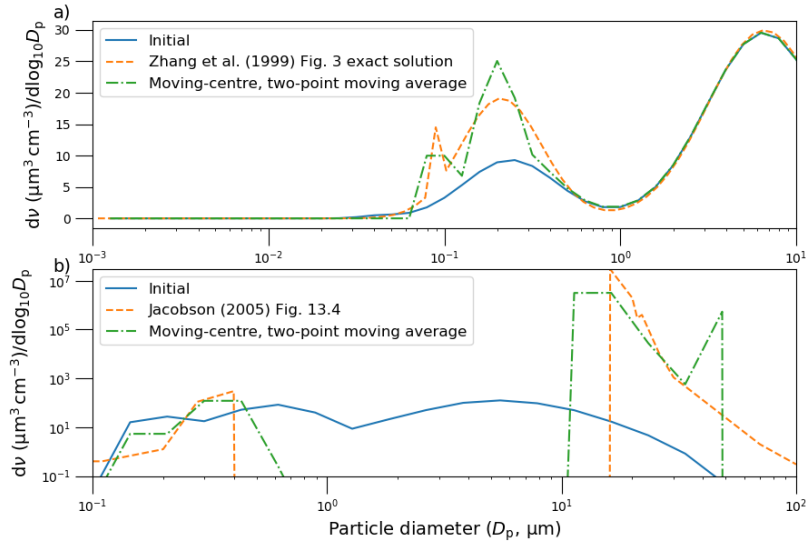


**Figure 7.** In a), replication of Fig.3 of Zhang et al. (1999) where a constant influx of sulphuric acid condenses to seed particles with the shown initial volume-size distribution, with final results shown after 12 hours. In b), replication of Fig. 13.8 of Jacobson (2005), where an initial distribution of particles are subject to a relative humidity of 100.002 % at minute intervals for 9 minutes, with results shown after 10 minutes.

Another case of relatively intense vapour-particle partitioning is provided by the example of cloud condensation nuclei experiencing varying degrees of water vapour supersaturation. Chamber experiments may involve injections of a component at specific times and the model variables input file can take such a scenario as input. Making use of this function we reproduce the benchmark simulation of Jacobson (2005) (Fig. 13.8) where relative humidity is increased to 100.002 % every minute (including at simulation start) for nine minutes, with results analysed after ten minutes. Seed particles are assumed non-volatile and wall interactions are turned off. Parameters such as temperature and the degree of dissociation, molecular weight and density of the seed particle are not disclosed by the reference simulation, therefore we set these as: 318.15 K, 1.0, 200  $\text{g mol}^{-1}$  and 1  $\text{g cm}^{-3}$ , respectively. The comparison between the Jacobson (2005) result in Fig. 7b and PyCHAM certainly shows agreement in the main feature of this simulation, which is the initially larger particles out competing smaller particles for water condensation to grow to water droplet size ( $D_p > 10 \mu\text{m}$ ). The PyCHAM result gives reasonable agreement considering that key parameters (such as seed component dissociation) may vary between simulations and taken together with Fig. 7a verifies the operation of gas-particle partitioning and the moving-centre structure.

## 8 Coagulation

Equations of coagulation kernels for Brownian diffusion, convective Brownian diffusion enhancement, gravitational collection, turbulent inertial motion, turbulent shear and Van der Waals collision were taken from Jacobson (2005). The unit test `test_coag` produces a plot of coagulation kernels that can be compared to Fig. 15.7 of Jacobson (2005) to verify its accuracy. Once the coagulation kernel for each pair of particle size bins ( $\beta$ ) has been found, the combinations of size bins (denoted  $j$  and  $z$ ) whose coagulation produces a particle of size bin  $k$  are identified:

$$Vb_{l,k} \leq (V_{j,t-h} + V_{z,t-h}) < Vb_{u,k}, \quad (8)$$

where  $V$  is particle volume,  $Vb_{l,k}$  and  $Vb_{u,k}$  are the lower and upper volume bounds of the size bin and  $h$  is the time step for coagulation to occur over. The semiimplicit coagulation equation from Jacobson (2005) is then used to estimate the new number concentration per size bin ( $N$  ( $\# \text{cm}^{-3}$ )):

$$N_{k,t} = \frac{N_{k,t-h} + \frac{1}{2}h \sum_{j=1}^{j_{max}} \beta_{z,j} N_{z,t} N_{j,t-h}}{1 + h \sum_{j=1}^{\infty} \beta_{k,j} N_{j,t-h}}, \quad (9)$$

where  $j_{max}$  is the largest size bin that can undergo coagulation to produce a particle in size bin  $k$ . This equation is not mass-conserving, however, the mass transfer between size bins is estimated using the number fraction of particles coagulating. For example, for a size bin  $k$ , the gain in molecular concentration of component  $i$  due to coagulation between size bins  $j$  and  $z$  (according to Eq. 8 and Eq. 9):

$$\Delta C_{i,k} = \frac{h(\frac{1}{2}\beta_{z,j} N_{z,t} N_{j,t-h} + \frac{1}{2}\beta_{j,z} N_{j,t} N_{z,t-h})}{N_{j,t-h}} C_{i,j,t-h}, \quad (10)$$

and the loss of molecular concentration from size bin  $k$  due to coagulation is:

$$\Delta C_{i,k} = - \left( 1 - \frac{1}{1 + h \sum_{j=1}^{\infty} \beta_{k,j} N_{j,t-h}} \right) C_{i,k,t-h}, \quad (11)$$

Eqs. 9- 11 show that coagulation directly influences the particle number- and mass-size distributions. We now assess the sensitivity of the number size distribution and mass conservation to the resolution of the operator-split time interval, and spatial resolution. A relatively complex initial distribution with four number modes is taken from ambient observations at Claremont, California on August 27, 1987 (Jacobson, 2005) and assumed to comprise non-volatile material. Results are presented for a six hour simulation in Fig. 8 where particle wall loss was turned off to allow clearer assessment of the coagulation sensitivity. In the top row of Fig. 8 no gas-phase chemistry was allowed, whilst in the bottom row, a single chemical reaction with reaction rate  $5.6 \times 10^{-17} \text{ molec}^{-1} \text{s}^{-1}$  between  $\alpha$ -pinene and O<sub>3</sub> (both with initial concentrations 100 ppb) was modelled to produce a single low volatility product with saturation vapour pressure of  $1 \times 10^{-10} \text{ Pa}$ , whilst gas-wall partitioning was turned off. For

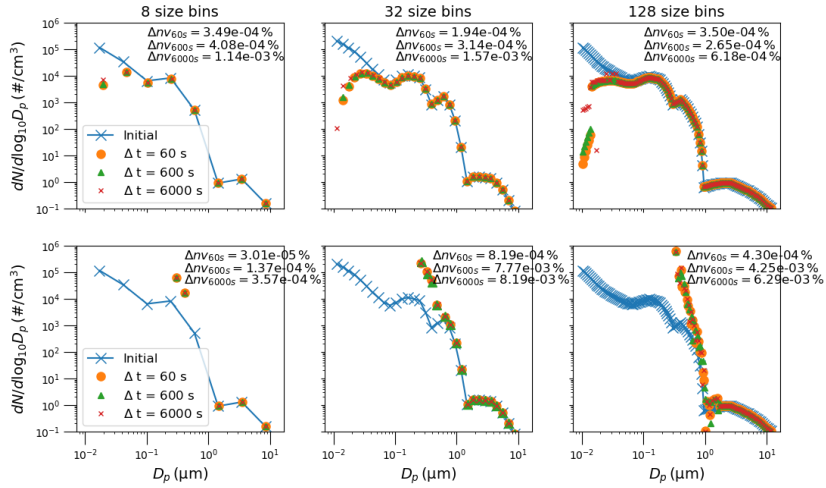


**Figure 8.** Sensitivity of the coagulation process to changes in operator-split temporal resolution (given in the legend) and spatial resolution (given in column titles). In the top row no chemistry occurred whilst in the bottom row a semi-volatile species was produced, as detailed in the main text. Results are for the end of a simulated six hour experiment. The  $\Delta nv_{\text{temporal resolution}}$  value given in the inset text is the percentage change in total non-volatile particle-phase material from the start to finish of the experiment, demonstrating mass conservation in the model.

the chemistry case, approximately  $500 \mu\text{g m}^{-3}$  of secondary material was formed, compared to  $90 \mu\text{g m}^{-3}$  of seed material. Columns in Fig. 8 are distinguished by the size bin resolution as presented in the column titles, and within each plot temporal resolution is varied.

The inset text of Fig. 8 ( $\Delta nv$ ) gives the fractional change in non-volatile material from the start to end (six hours) of the simulation for the three temporal resolutions. It is clear that the coagulation equations introduce negligible error to mass conservation. Two features are present in the top row (no chemistry) of Fig. 8: first, that in terms of number concentration, coagulation overwhelmingly affects the number concentration of smaller particles - note that such particles are sufficiently small in volume that they may coagulate with a larger particle without causing it to grow a size bin; second, that only for the smallest particles (below a diameter of  $3 \times 10^{-2} \mu\text{m}$  in this case) is a sensitivity to temporal resolution clear across all size bin resolutions. For the no chemistry case there is demonstrable coupling of spatial and temporal resolution, with an increase in the former indicating greater sensitivity to the latter. However, all the resolution considerations above become redundant when we consider the case with gas-particle partitioning (bottom row of Fig. 8). In this instance, the effect of partitioning dominates the change in number-size distribution and no sensitivity of coagulation to spatial or temporal resolution is discernible. We recommend users consider these examples in addition to the nature of their simulation and objective when deciding whether temporal or spatial resolution will significantly impact results.



## 9 Particle deposition to walls

As with gas-wall partitioning, the loss of particles to chamber walls can significantly invalidate chamber results if unaccounted for and has been detailed in previous publications (Crump and Seinfeld, 1981; McMurry and Rader, 1985; Nah et al., 2017; Wang et al., 2018). During control experiments the deposition rate of particles to walls can be inferred through observations of the rate of decay of particles of varying size (with coagulation accounted for) (Charan et al., 2019). Several studies have published results from such experiments (McMurry and Rader, 1985; Wang et al., 2018), including a relatively large dataset from the EUROCHAMP2020 project (Oliveri, 2018). Comparison of inferred wall loss rates indicate that relatively small and larger particles have higher loss rates due diffusion and settling (Crump and Seinfeld, 1981), respectively, however the absolute values and size-dependent gradient of the loss rates vary significantly between control experiments. Even for a given chamber, significant variations appear with changes to relative humidity, disturbance to walls due to air conditioning, and, for teflon chambers, with time since the chamber walls experienced frictional force to create electrostatic charge (Wang et al., 2018). Currently no method is available to measure the required inputs that a particle deposition model would need to satisfactorily reproduce observations across all chambers and conditions, therefore in PyCHAM users have three options to estimate particle wall deposition. Here we describe the options and provide examples of their use.

Users select wall loss treatment with the `McMurry_flag` option in the model variables input file. The default (if left empty) is no loss of particles to wall, which can be used for estimating wall loss corrected values such as aerosol yield. If set to 1, the model of McMurry and Rader (1985) is used, which is based on the particle deposition model of Crump and Seinfeld (1981) but with electrostatic effects. Studies have found the Crump and Seinfeld (1981) and McMurry and Rader (1985) approach to reproduce measured particle wall losses well (Chen et al., 1992; Kim et al., 2001). Selecting McMurry and Rader (1985) requires the user to also input the chamber surface area, the average charge per particle and the average electric field inside the chamber, where the latter two may be set to zero for nullifying electrostatic effects. With the `test_wallloss` module users can confirm that PyCHAM accurately reproduces Fig. 2 of McMurry and Rader (1985), as shown here in Fig. 9, which demonstrates the effect of changing the charge number per particle.

If user sets the `McMurry_flag` option to 0 then a customised particle deposition rate dependence on particle size is available. This option allows application of known or best estimate deposition rates ( $\beta$ ) to the model, as recommended by Wang et al. (2018). Four further inputs are required for this option: the particle diameter at which the inflection in deposition rates occurs ( $D_{p, flec}$ ) (where the inflection point marks a change in dependance of deposition rate with particle size), the rate of particle deposition to wall at the inflection point ( $\beta_{flec}$ ), and the gradients of the deposition rate with respect to particle diameter before ( $\nabla_{pre}$ ) and after the inflection ( $\nabla_{pro}$ ), where a linear dependence in log-log space is assumed, consistent with observations (Charan et al., 2019). The equations for deposition rate in this instance are given in Eq. 12, and example dependencies of rate with particle size provided by Fig. 9.

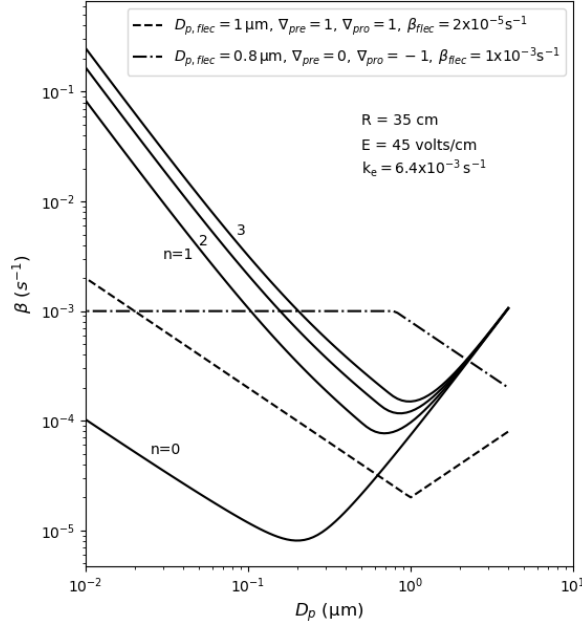


**Figure 9.** Example dependencies of the particle deposition to wall rate using the model of McMurry and Rader (1985) in the solid lines, where the charge per particle is given by  $n$  and other inputs given by inset text ( $R$  is spherical-equivalent chamber radius,  $E$  is the average electric field in the chamber and  $k_e$  is the coefficient of eddy diffusion). The dashed lines demonstrate the the observation-based deposition rate utility of PyCHAM given in Eq. 12, with inputs at the top of the plot.

$$D_p < D_{p,flec}$$

$$\log_{10}(\beta(D_p)) = \log_{10}(D_{p,flec}) - \log_{10}(D_p)\nabla_{pre} + \beta_{flec}$$

$$D_p \geq D_{p,flec}$$

$$\log_{10}(\beta(D_p)) = \log_{10}(D_p) - \log_{10}(D_{p,flec})\nabla_{pro} + \beta_{flec} \quad (12)$$

## 10 Nucleation

The simulation of nucleation to produce newly-formed suspended particles is an area of ongoing research (e.g. Kurten et al., 2018; Semeniuk and Dastoor, 2018; Li et al., 2020). To date, there is not a generally acceptable model. Consequently, for

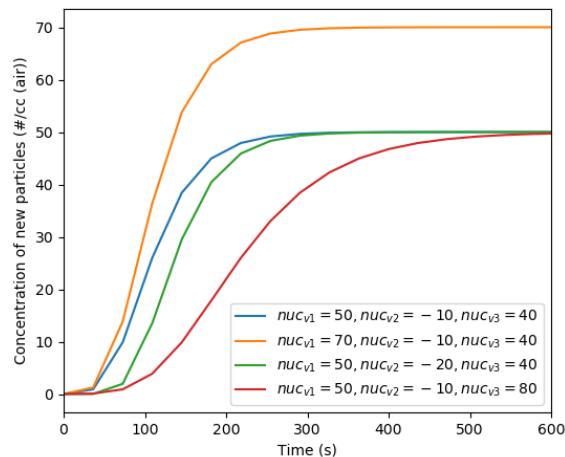


**Figure 10.** Effect of varying the nucleation parameters on simulated particle number concentration when considering only nucleation.

PyCHAM simulations involving nucleation, users are able to provide parameters to a Gompertz function for cumulative new particle number, allowing them to fit to observed number size distributions:

$$P_1(t) = \text{nuc}_{v1} (\exp(\text{nuc}_{v2} (\exp(-t/\text{nuc}_{v3})))) \quad (13)$$

where  $P_1$  is the number concentration of new particles after time  $t$  that enter the smallest size bin, and  $\text{nuc}_{vn}$  are the user-defined parameters. The resulting function forms an asymmetrical sigmoidal curve with time, whilst the parameters allow the amplitude ( $\text{nuc}_{v1}$ ), onset ( $\text{nuc}_{v2}$ ), and duration ( $\text{nuc}_{v3}$ ) of the curve to be adjusted, as shown in Fig. 10. The Gompertz function provides a sigmoidal form with faster increase in new particle number prior to peak rate of production than after (Fig. 10). This form is provided as our testing has indicated it gives better fits to number size distribution than a symmetrical sigmoidal function.

To obtain the nucleation parameters that most accurately fit measurements, number size distribution measurements provide a relatively detailed indicator of fit, whilst total particle number concentration is less informative and therefore less able to provide constraint.

Although it is accepted that clusters of molecules are responsible for forming the nucleus of a particle (Seinfeld and Pandis, 2006), the shape and spherical-equivalent radius of these is uncertain. Inside the model variables file the radius of newly nucleated particles is set by the user. Using the volume equation for the cluster's assumed spherical shape and the molar volume of the component assumed responsible for nucleation (also set by the user), the molar concentration of nucleating component required is calculated and added to the smallest size bin of the particle phase whilst subtracted from the vapour phase. The average radius of the particles in this size bin is then calculated by dividing the total volume of molecules by the number of particles (including those present prior to nucleation). With the Kelvin effect estimated to be relatively large

420 at typical nucleation cluster sizes, the model is very sensitive to the input radius of new particles and the volatility of the nucleating component. Above a certain vapour pressure (dependent on particle size and the propensity of other components to condense), the nucleating component will undergo net evaporation during the gas-particle partitioning solution, and possibly invoke the moving-centre structure to reduce the integration time step toward zero seconds (as explained in Section 7).

## 11 Sensitivity to Temporal Resolution

425 The operator-split processes of coagulation, particle loss to walls and nucleation all affect the number size distribution of particles and in turn the concentration of SOA. Whilst the temporal resolution used for these processes can be decreased to decrease the time required for simulation, it can also introduce inaccuracies to results. Although it is beyond the scope of this paper to assess temporal resolution sensitivity across all possible PyCHAM parameter space, in this section we compare the divergence of outputs from simulations with decreasing temporal resolution against a high temporal resolution reference for  
430 extremes of the relevant parameter space: seeded experiments with no gas-particle partitioning and both seeded and nucleation experiments with relatively intense gas-particle partitioning. Results here determine the recommended temporal resolution, provide a useful illustration of sensitivity and may help users perform sensitivity tests for their individual model inputs.

For the no partitioning simulations, particle number size distribution and total number concentration are considered, whilst for the partitioning simulations, concentration of secondary material is also relevant. For number size distribution, absolute  
435 divergence ( $|\% \Delta|$ ) is calculated as an average over size bins containing particles and time steps, with  $Y$  of the former and  $Z$  of the latter:

$$|\% \Delta| = \frac{\sum_{t_i=1}^{t_i=Z} \sum_{k=1}^{k=Y} \frac{|(n_{t_i,k} - \bar{n}_{t_i,k})|}{\vee(n_{t_i,k}, \bar{n}_{t_i,k})}}{ZY} 100, \quad (14)$$

where  $n_{t_i,k}$  is the particle number concentration at time step  $t_i$  in size bin  $k$  from a lower temporal resolution simulation and  $\bar{n}_{t_i,k}$  is the output from the reference maximum temporal resolution simulation. Where the two agree exactly the contribution  
440 to  $|\% \Delta|$  is zero, and where one output is zero and the other is greater,  $|\% \Delta|$  is at a maximum of 100. The term  $\vee(n_{t_i,k}, \bar{n}_{t_i,k})$  means the greater of  $n_{t_i,k}$  and  $\bar{n}_{t_i,k}$  is used as denominator.

For total number concentration and total secondary material concentration, divergence is calculated as the percentage deviation averaged over time steps:

$$|\% \Delta| = \frac{\sum_{t_i=1}^{t_i=Z} \frac{|(N_{t_i} - \bar{N}_{t_i})|}{\vee(N_{t_i}, \bar{N}_{t_i})}}{Z} 100, \quad (15)$$

445 where  $N$  represents either total number concentration or total secondary material concentration. Simulation start time is not included in the divergence calculation, as outputs are necessarily identical. Results from the low temporal resolution cases are linearly interpolated to the output times of the high resolution reference case to allow comparison.

For all sensitivity simulations, 128 logarithmically spaced size bins are used, for which Fig. 8 indicates no limitation to accuracy due to spatial resolution. For seeded simulations, we use the same initial number size distribution as in Fig. 8, as  
 450 this gives a relatively broad range of particle sizes, which is necessary to fully appreciate the size-dependent effects of the operator-split processes. All simulations were run for 24 hours and the reference simulation had an operator-split time step of 6 s.

Results are shown across three plots. The first, given in Fig. 11a) represents the no partitioning case, with sensitivity assessed for two setups: only coagulation, and both coagulation and wall loss turned on. Coagulation proceeds as described in Section 8, whilst wall loss is described in Section 9, with the following inputs to recreate a size-dependent wall loss profile similar to  $n=3$   
 455 in Fig. 9:  $D_{p, flec} = 1.0 \mu\text{m}$ ,  $\beta_{flec} = 1.0 \times 10^{-4} \text{ s}^{-1}$ ,  $\nabla_{pre} = \nabla_{pro} = 1.5$ . Consequently, the particle loss to wall is relatively intense and the sensitivity results are conservative. Fig. 11a) indicates that under this scenario, particle loss to walls considerably increases sensitivity to temporal resolution, with average deviations of 10 % for both total particle number concentration and number size distribution occurring at resolutions around two orders of magnitude finer than for coagulation alone.

For Fig. 11b), two-methylglyceric acid is introduced at a rate of  $1.0 \times 10^{-2} \text{ ppbs}^{-1}$  and increases sensitivity to temporal resolution compared to Fig. 11a). A resolution of around 60 s is required to attain divergences less than 10 % for total number concentrations and secondary material, whilst for number size distribution, not even the lowest temporal resolution of 12 s can produce average divergence below 10 % when compared against the reference case of 6 s. This reflects the steep gradients in particle size-number space that are generated during intense partitioning periods, such as those produced in Fig. 7, since small  
 465 changes to the operator-split time step can lead to slight variations in the size bins that particles concentration in. This effect is even further pronounced when a generic extremely low volatility organic component is injected at the simulation start at 1 ppb to act as a nucleating agent with no seed aerosol present, with results given in Fig. 11c). We use the nucleation parameters for Eq. 13 of:  $nuc_{v1} = 1 \times 10^4$ ,  $nuc_{v2} = -10$  and  $nuc_{v3} = 100$ , for a relatively intense nucleation period (lasting only ten minutes) and therefore conservative assessment of sensitivity. However, Fig. 11c) indicates that although the particle may not be in the  
 470 same size bin as the reference case, the total concentration of number and secondary material diverges from the reference case by around 10 % for an operator-split time step of 60 s. Given the conservative nature of these simulations we therefore recommend a maximum operator-split time step of 60 s.

## 12 Conclusions

The PyCHAM (CHemistry with Aerosol Microphysics in Python) software for aerosol chambers has been described. Its open-  
 475 source repository is given in Section 1. PyCHAM has been designed for optimal ease of use (from download to output) whilst observing the latest scientific findings relevant to the full range of aerosol chambers (Section 2). We have provided a model output for the dark oxidation of limonene to illustrate the coupling of modelled processes: gas-phase chemistry, gas-particle partitioning, gas-wall partitioning, redistribution of particles between size bins, particle loss to wall, coagulation and nucleation (Sections 2 and 3).

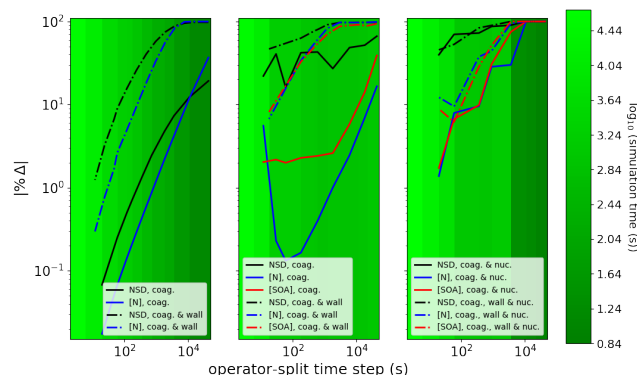


**Figure 11.** Sensitivity of number size distribution (NSD), total particle number concentration ([N]) and total concentration of secondary material ([SOA]) to operator-split temporal resolution. In plots a) and b), coagulation (coag.) and particle loss to wall (wall) are probed, whilst in c) nucleation (nuc.) is additionally probed. In a) no gas-particle partitioning is allowed, whilst in b) and c) it is, as two-methylglyceric acid is continuously injected at a rate of  $1.0 \times 10^{-2}$  ppbs $^{-1}$ . Also in c) a generic extremely low volatility organic component is present at simulation start at 1 ppb, and is set as the nucleating component. Contours represent the time taken for simulation.

480 The steps to run a simulation using the software’s GUI were described in Section 3 and the methods for estimating or setting component properties explained in Section 4. The setting up and solution of gas-phase photochemical reactions is detailed in Section 5, including comparison against the AtChem2 model (Sommariva et al., 2018) for verification and illustration of the effect of varying the boundary condition time interval on model output for a system subject to varying natural light intensity.

For gas-wall partitioning this paper details (Section 6) a parameterisation that aims to satisfy the breadth of chamber characteristics and recommends a method for tuning to observations. In Section 7, gas-particle partitioning and the moving-centre structure for redistributing particles between size bins was introduced and verified against benchmark simulations.

Coagulation was detailed in Section 8 and shown to introduce negligible loss of mass conservation. With Section 9, the three options for treating particle losses to walls were detailed and the resulting deposition rates as a function of particle diameter were exemplified, including verification against the benchmark of McMurry and Rader (1985). Similar to gas-wall partitioning, nucleation in PyCHAM is treated with a parameterisation that aims to optimise model versatility, with examples of parameter effects provided (Section 10).

In Section 11 the sensitivity of key outputs to varying operator-split temporal resolution was illustrated. RECOMMENDATION ON TEMPORAL RESOLUTION TO USE HERE.

Throughout the paper guidance and details on the use of PyCHAM is provided. Furthermore, the applicability of the software to a wide variety of chamber experiments is a continuous theme, true to the software design.

*Code and data availability.*

The PyCHAM software, figures in this manuscript, PyCHAM inputs to create figures and code to plot figures is available at:  
<https://github.com/simonom/PyCHAM>

## Appendix A

500 **A1**

*Author contributions.* Gordon McFiggans was principal investigator for the PyCHAM project. Simon O'Meara and Shuxuan Xu equally contributed to writing of the PyCHAM software. David Topping wrote the PyBOX software, Douglas Lowe and Gerard Capes wrote the MANIC software, both MANIC and PyBOX were used as starting points for PyCHAM. Rami Alfarra provided guidance on chamber experiments. Simon O'Meara wrote this manuscript, with edits provided equally from all other authors.

505 *Competing interests.* The authors declare no competing interests.

*Disclaimer.* The PyCHAM software is provided under the GNU General Public License v3.0.

*Acknowledgements.* This project has received funding from the European Union's Horizon 2020 research and innovation programme under grant agreement No 730997. Simon O'Meara has received funding from the National Centre for Atmospheric Science.

## References

- Andersson, C., Führer, C., and Åkesson, J.: Assimulo: A unified framework for {ODE} solvers, *Mathematics and Computers in Simulation*, 116, 26 – 43, <https://doi.org/http://dx.doi.org/10.1016/j.matcom.2015.04.007>, 2015.
- Barley, M., Topping, D., and McFiggans, G.: Critical Assessment of Liquid Density Estimation Methods for Multifunctional Organic Compounds and Their Use in Atmospheric Science, *J. Phys. Chem. A*, 117, 3428–3441, <https://doi.org/10.1021/jp304547r>, 2013.
- Carslaw, N. and Shaw, D.: Secondary product creation potential (SPCP): a metric for assessing the potential impact of indoor air pollution on human health, *ENVIRONMENTAL SCIENCE-PROCESSES & IMPACTS*, 21, 1313–1322, <https://doi.org/10.1039/c9em00140a>, 2019.
- Charan, S. M., Huang, Y., and Seinfeld, J. H.: Computational Simulation of Secondary Organic Aerosol Formation in Laboratory Chambers, *Chemical reviews.*, 119, 11 912,11 944, <https://doi.org/10.1021/acs.chemrev.9b00358>, 2019.
- Chen, B. T., Yeh, H. C., and Cheng, Y. S.: Evaluation of an Environmental Reaction Chamber, *Aerosol Sci. Tech.*, 17, 9–24, <https://doi.org/10.1080/02786829208959556>, 1992.
- Crump, J. G. and Seinfeld, J. H.: Turbulent deposition and gravitational sedimentation of an aerosol in a vessel of arbitrary shape, *J. Aerosol Sci.*, 12, 405–415, [https://doi.org/10.1016/0021-8502\(81\)90036-7](https://doi.org/10.1016/0021-8502(81)90036-7), 1981.
- Day, D. A., Ziemann, P. J., Jimenez, J. L., Krechmer, J. E., Day, D. A., Ziemann, P. J., and Jimenez, J. L.: Direct Measurements of Gas/Particle Partitioning and Mass Accommodation Coefficients in Environmental Chambers, *Environ. Sci. Techol.*, 51, 11 867,11 875, 2017.
- Ehn, M., Thornton, J., Kleist, E., Sipilä, M., Junninen, H., Pullinen, I., Springer, M., Rubach, F., Tillmann, R., Lee, B., Lopez-Hilfiker, F., Andres, S., Acir, I., Rissanen, M., Jokinen, T., Schobesberger, S., Kangasluoma, J., Kontkanen, J., Nieminen, T., Kurtén, T., Nielsen, L. B., Jørgensen, S., Kjaergaard, H., Canagaratna, M., Maso, M., Berndt, T., Petäjä, T., Wahner, A., Kerminen, V., Kulmala, M., Worsnop, D., Wildt, J., and Mentel, T.: A large source of low-volatility secondary organic aerosol, *Nature*, 506, 476–479, <https://doi.org/10.1038/nature13032>, 2014.
- European Commission Environment: European Commission Directives on Air Quality, [https://ec.europa.eu/environment/air/quality/existing\\_leg.htm](https://ec.europa.eu/environment/air/quality/existing_leg.htm), 2020.
- Fry, J. L., Kiendler-Scharr, A., Rollins, A. W., Brauers, T., Brown, S. S., Dorn, H.-P., Dubé, W. P., Fuchs, H., Mensah, A., Rohrer, F., Tillmann, R., Wahner, A., Wooldridge, P. J., and Cohen, R. C.: SOA from limonene: role of NO<sub>3</sub> in its generation and degradation, *Atmos. Chem. Phys.*, 11, 3879–3894, <https://doi.org/10.5194/acp-11-3879-2011>, 2011.
- Fuchs, N. and Sutugin, A.: Highly dispersed aerosols, Butterworth Heinemann, Woburn, Mass, 1971.
- Girolami, G. S.: A Simple "Back of the Envelope" Method for Estimating the Densities and Molecular Volumes of Liquids and Solids, *Journal of chemical education.*, 71, 962–964, <https://doi.org/10.1021/ed071p962>, 1994.
- Griffin, C. W., Kantzes, H. L., Ludford, P. M., and Pelczar, M. J.: Studies of Aerosols with a Simple Cloud-Chamber Technic, *Applied and Environmental Microbiology*, 4, 17–20, <https://doi.org/10.1128/AEM.4.1.17-20.1956>, <https://aem.asm.org/content/4/1/17>, 1956.
- Hayman, G.: Effects of pollution control on UV Exposure, AEA Technology Final Report (Reference AEA/RCEC/22522001/R/002 ISSUE1) prepared for the Department of Health on Contract 121/6377, AEA Technology, Oxfordshire, UK, 1997.
- Heal, M., Kumar, P., and Harrison, R.: Particles, air quality, policy and health, *Chem. Soc. Rev.*, 41, 6606–6630, <https://doi.org/10.1039/c2cs35076a>, 2012.
- Hidy, G.: Atmospheric Chemistry in a Box or a Bag, *Atmosphere-Basel*, 10(7), <https://doi.org/10.3390/atmos10070401>, 2019.
- Hindmarsh, A. C., Brown, P. N., Grant, K. E., Lee, S. L., Serban, R., Shumaker, D. E., and Woodward, C. S.: SUNDIALS: Suite of nonlinear and differential/algebraic equation solvers, *ACM Transactions on Mathematical Software (TOMS)*, 31, 363–396, 2005.



- Jacobson, M.: Fundamentals of Atmospheric Modeling, Cambridge University Press, Cambridge, U.K., 2 edn., 2005.
- Jaoui, M., Lewandowski, M., Docherty, K., Offenberg, J. H., and Kleindienst, T. E.: Atmospheric oxidation of 1,3-butadiene: characterization of gas and aerosol reaction products and implications for PM 2.5, *Atmos. Chem. Phys.*, 14, 13 681–13 704, <https://doi.org/10.5194/acp-14-13681-2014>, 2014.
- 550 Jenkin, M., Saunders, S., and Pilling, M.: The tropospheric degradation of volatile organic compounds: A protocol for mechanism development, *Atmos. Env.*, 31, 81–104, [https://doi.org/10.1016/S1352-2310\(96\)00105-7](https://doi.org/10.1016/S1352-2310(96)00105-7), 1997.
- Johnson, J., Regayre, L., Yoshioka, M., Pringle, K., Lee, L., Sexton, D., Rostron, J., Booth, B., and Carslaw, K.: The importance of comprehensive parameter sampling and multiple observations for robust constraint of aerosol radiative forcing, *Atmos. Chem. Phys.*, 18, 13 031–13 053, <https://doi.org/10.5194/acp-18-13031-2018>, 2018.
- 555 Kim, H. O., Han, Y. T., Kwon, S. B., and Lee, K. W.: Wall Loss Rate of Polydispersed Aerosols, *Aerosol Sci. Tech.*, 35, 710–717, <https://doi.org/10.1080/02786820152546752>, 2001.
- Kurten, A., Li, C., Bianchi, F., Curtius, J., Dias, A., Donahue, N., Duplissy, J., Flagan, R., Hakala, J., Jokinen, T., Kirkby, J., Kulmala, M., Laaksonen, A., Lehtipalo, K., Makhmutov, V., Onnela, A., Rissanen, M., Simon, M., Sipila, M., Stozhkov, Y., Trostl, J., Ye, P., and McMurry, P.: New particle formation in the sulfuric acid-dimethylamine-water system: reevaluation of CLOUD chamber measurements and comparison to an aerosol nucleation and growth model, *Atmos. Chem. Phys.*, 18(2), 845–863, [https://doi.org/10.5194/acp-18-845-](https://doi.org/10.5194/acp-18-845-2018)  
560 2018, 2018.
- Li, D., Chen, D., Liu, F., , and Wang, W.: Role of glycine on sulfuric acid-ammonia clusters formation: Transporter or participator, *J. Environ. Sci.*, 89, 125–135, <https://doi.org/10.1016/j.jes.2019.10.009>, 2020.
- Lowe, D., Archer-Nicholls, S., Morgan, W., Allan, J., Utembe, S., Ouyang, B., Aruffo, E., Le Breton, M., Zaveri, R. A., Di Carlo, P., Percival, C., Coe, H., Jones, R., and McFiggans, G.: WRF-Chem model predictions of the regional impacts of N2O5 heterogeneous processes on night-time chemistry over north-western Europe, *Atmospheric chemistry and physics : ACP.*, 15, 1385–1409, [https://doi.org/10.5194/acp-](https://doi.org/10.5194/acp-15-1385-2015)  
565 15-1385-2015, 2015.
- Lowe, D., Topping, D., and McFiggans, G.: Modelling multi-phase halogen chemistry in the remote marine boundary layer: investigation of the influence of aerosol size resolution on predicted gas- and condensed-phase chemistry, *ATMOSPHERIC CHEMISTRY AND PHYSICS*, 9, 4559–4573, <https://doi.org/10.5194/acp-9-4559-2009>, 2009.
- 570 Matsunaga, A. and Ziemann, P.: Gas-Wall Partitioning of Organic Compounds in a Teflon Film Chamber and Potential Effects on Reaction Product and Aerosol Yield Measurements, *Aerosol Sci. Tech.*, <https://doi.org/10.1080/02786826.2010.501044>, 2010.
- McMurry, P. and Rader, D.: Aerosol Wall Losses in Electrically Charged Chambers, *Aerosol Sci. Tech.*, 4, 249 – 268, <https://doi.org/10.1080/02786828508959054>, 1985.
- 575 Meng, Z., Dabdub, D., and Seinfeld, J. H.: Chemical Coupling Between Atmospheric Ozone and Particulate Matter, *Science.*, 277, 116,119, <https://doi.org/10.1126/science.277.5322.116>, 1997.
- MIT Science and Policy of Global Change: MIT Joint Program on the Science and Policy of Global Change, <https://globalchange.mit.edu/publications>, 2020.
- Nah, T., McVay, R. C., Pierce, J. R., Seinfeld, J. H., and Ng, N. L.: Constraining uncertainties in particle-wall deposition correction during SOA formation in chamber experiments, *Atmos. Chem. Phys.*, 17, 2297–2310, <https://doi.org/10.5194/acp-17-2297-2017>, 2017.
- 580 Nannoolal, Y., Rarey, J., and Ramjugernath, D.: Estimation of pure component properties Part 3. Estimation of the vapour pressure of non-electrolyte organic compounds via group contributions and group interactions, *Fluid Phase Equilibr.*, 269, 117–133, <https://doi.org/10.1016/j.fluid.2008.04.020>, 2008.

- Naumann, K.-H.: COSIMA - a computer program simulating the dynamics of fractal aerosols, *J. Aerosol. Sci.*, 34, 1371–1397, [https://doi.org/10.1016/S0021-8502\(03\)00367-7](https://doi.org/10.1016/S0021-8502(03)00367-7), 2003.
- O’Boyle, N., Banck, M., James, C., Morley, C., Vandermeersch, T., and Hutchinson, G.: Open Babel: An open chemical toolbox, *J Cheminformatics*, 3, <https://doi.org/10.1186/1758-2946-3-33>, 2011.
- Odum, J., Hoffmann, T., Bowman, F., Collins, D., Flagan, R., and Seinfeld, J.: Gas-particle partitioning and secondary organic aerosol yields, *Environ. Sci. Technol.*, 30, 2580–2585, <https://doi.org/10.1021/es950943+>, 1996.
- Oliveri, M.: EUROCHAMP 2020, <https://www.eurochamp.org/Eurochamp2020.aspx>, 2018.
- O’Meara, S., Booth, A., Barley, M., Topping, D., and McFiggans, G.: An assessment of vapour pressure estimation methods, *Phys. Chem. Chem. Phys.*, 16, 19453–19469, <https://doi.org/10.1039/c4cp00857j>, 2014.
- O’Meara, S., Xu, S., Topping, D., Capes, G., Lowe, D., Alfarrá, M., and McFiggans, G.: PyCHAM: CHemistry with Aerosol Microphysics in Python, *Journal of Open Source Software*, 5, 1918, <https://doi.org/10.21105/joss.01918>, 2020.
- Pierce, J., Englehart, G., Hildebrandt, L., Weitkamp, E., Parthak, E., and Donahue, N.: Constraining Particle Evolution from Wall Losses, Coagulation and Condensation-Evaporation in Smog Chamber Experiments: Optimal Based Size Distribution Measurements, *Aerosol Sci. Tech.*, 42, <https://doi.org/10.1080/02786820802389251>, 2008.
- Rickard, A. and Young, J.: The Master Chemical Mechanism, <http://mcm.leeds.ac.uk/MCM/>, 2020.
- Riva, M., Heikkinen, L., Quelever, L., Roldin, P., Peräkylä, O., Quéléver, L., and Ehn, M.: Experimental investigation into the volatilities of highly oxygenated organic molecules (HOMs), *Atmospheric chemistry and physics : ACP.*, 20, 649,669, <https://doi.org/10.5194/acp-20-649-2020>, 2020.
- Roldin, P., Ericsson, A., Nordin, E., Hermansson, E., Mogensen, D., Rusanen, A., Boy, M., Swietlicki, E., Svenningsson, B., Zelenyuk, A., and Pagels, J.: Modelling non-equilibrium secondary organic aerosol formation and evaporation with the aerosol dynamics, gas- and particle-phase chemistry kinetic multilayer model ADCHAM, *Atmos. Chem. Phys.*, 14, <https://doi.org/10.5194/acp-14-7953-2014>, 2014.
- Roldin, P., Ehn, M., Kurtén, T., Olenius, T., Rissanen, M., Sarnela, N., Elm, J., Rantala, P., Hao, L., Hyttinen, N., Heikkinen, L., Worsnop, D., Pichelstorfer, L., Xavier, C., Clusius, P., Öström, E., Petäjä, T., Kulmala, M., Vehkamäki, H., Virtanen, A., Riipinen, I., and Boy, M.: The role of highly oxygenated organic molecules in the Boreal aerosol-cloud-climate system, *Nat. Commun.*, 10, <https://doi.org/10.1038/s41467-019-12338-8>, 2019.
- Saunders, S. M., Jenkin, M. E., Derwent, R., and Pilling, M. J.: Protocol for the development of the Master Chemical Mechanism, MCM v3 (Part A): tropospheric degradation of non-aromatic volatile organic compounds, *Atmos. Chem. Phys.*, 3, 161–180, <https://doi.org/10.5194/acp-3-161-2003>, 2003.
- Schwantes, R., McVay, R., Zhang, X., Coggon, M., Lignell, H., Flagan, R., Wennberg, P., and Seinfeld, J.: Advances in Atmospheric Chemistry, Chapter 1: Science of the Environmental Chamber, World Scientific, <https://doi.org/10.1142/10216>, 2017.
- Seinfeld, J. and Pandis, S.: Atmospheric chemistry and physics: from air pollution to climate change, Wiley, Hoboken, N.J., 2 edn., 2006.
- Semeniuk, K. and Dastoor, A.: Current state of aerosol nucleation parameterizations for air-quality and climate modeling, *Atmos. Environ.*, 179, 77–106, <https://doi.org/10.1016/j.atmosenv.2018.01.039>, 2018.
- Sommariva, R., Cox, S., Martin, C., Boronska, K., Young, J., Jimack, P., Pilling, M. J., Bloss, W. J., Monks, P. S., and Rickard, A. R.: AtChem, an open source box-model for the Master Chemical Mechanism, in: Atmospheric Chemical Mechanisms Conference, 2018.
- Stefenelli, G., Pieber, S. M., Bruns, E. A., Temime-Roussel, B., Bertrand, A., Pieber, S. M., Bruns, E. A., Slowik, J. G., Wortham, H., Prévôt, A. S. H., El Haddad, I., and Marchand, N.: Influence of the vapor wall loss on the degradation rate constants in chamber experiments of levoglucosan and other biomass burning markers, *Atmos. Chem. Phys.*, 18, 10915,10930, 2018.

- Sunol, A., Charan, S., and Seinfeld, J.: Computational simulation of the dynamics of secondary organic aerosol formation in an environmental chamber, *Aerosol Sci. Tech.*, 52, 470 – 482, <https://doi.org/10.1080/02786826.2018.1427209>, 2018.
- Surratt, J. D., Murphy, S. M., Kroll, J. H., Ng, N. L., Hildebrandt, L., Sorooshian, A., Szmigielski, R., Vermeylen, R., Maenhaut, W., Claeys, M., Flagan, R. C., and Seinfeld, J. H.: Chemical Composition of Secondary Organic Aerosol Formed from the Photooxidation of Isoprene, *J. Phys. Chem-US*, 110, <https://doi.org/10.1021/jp061734m>, 2006.
- Tong, D., Geng, G., Jiang, K., Cheng, J., Zheng, Y., Hong, C., Yan, L., Zhang, Y., Chen, X., Bo, Y., Lei, Y., Zhang, Q., and He, K.: Energy and emission pathways towards PM<sub>2.5</sub> air quality attainment in the Beijing-Tianjin-Hebei region by 2030, *Sci. Total Environ.*, 692, 361–370, <https://doi.org/10.1016/j.scitotenv.2019.07.218>, 2019.
- Topping, D., Barley, M., Bane, M. K., Higham, N., Aumont, B., Dingle, N., and McFiggans, G.: UManSysProp v1.0: an online and open-source facility for molecular property prediction and atmospheric aerosol calculations, *Geoscientific Model Development*, 9, 899–914, <https://doi.org/10.5194/gmd-9-899-2016>, <https://www.geosci-model-dev.net/9/899/2016/>, 2016.
- Topping, D., Connolly, P., and Reid, J.: PyBOX: An automated box-model generator for atmospheric chemistry and aerosol simulations, *The Journal of Open Source Software*, 3(28), <https://doi.org/10.21105/joss.00755>, 2018.
- UK Government: Environment Bill 2020, <https://www.gov.uk/government/publications/environment-bill-2020>, 2020.
- UNFCCC: Paris Agreement, [https://unfccc.int/sites/default/files/english\\_paris\\_agreement.pdf](https://unfccc.int/sites/default/files/english_paris_agreement.pdf), 2018.
- Wang, N., Jorga, S., Pierce, J., Donahue, N., and Pandis, S.: Particle wall-loss correction methods in smog chamber experiments, *Atmos. Meas. Tech.*, 11, 6577 – 6588, <https://doi.org/10.5194/amt-11-6577-2018>, 2018.
- Waring, M. S. and Wells, J. R.: Volatile organic compound conversion by ozone, hydroxyl radicals, and nitrate radicals in residential indoor air: Magnitudes and impacts of oxidant sources, *ATMOSPHERIC ENVIRONMENT*, 106, 382–391, <https://doi.org/10.1016/j.atmosenv.2014.06.062>, 2015.
- Weininger, D.: Smiles, a chemical language and information system. 1. Introduction to methodology and encoding rules, *J. Chem. Inf. Comp. Sci.*, 28, 31–36, <https://doi.org/10.1021/ci00057a005>, 1988.
- Ying, Q. and Li, J.: Implementation and initial application of the near-explicit Master Chemical Mechanism in the 3D Community Multiscale Air Quality (CMAQ) model, *Atmospheric Environment*, 45, 3244 – 3256, <https://doi.org/https://doi.org/10.1016/j.atmosenv.2011.03.043>, <http://www.sciencedirect.com/science/article/pii/S1352231011003037>, 2011.
- Zaveri, R., Easter, R., Fast, J., and Peters, L.: Model for Simulating Aerosol Interactions and Chemistry (MOSAIC), *J. Geophys. Res.*, 113, D13 204, <https://doi.org/10.1029/2007JD008782>, 2008.
- Zhang, X., Schwantes, R., McVay, R., Lignell, H., Coggon, M., Flagan, R., and Seinfeld, J.: Vapor wall deposition in Teflon chambers, *Atmos. Chem. Phys.*, 15, 4197–4214, <https://doi.org/10.5194/acp-15-4197-2015>, 2015.
- Zhang, Y., Seigneur, C., Seinfeld, J. H., Jacobson, M. Z., and Binkowski, F. S.: Simulation of Aerosol Dynamics: A Comparative Review of Algorithms Used in Air Quality Models, *Aerosol science and technology.*, 31, 487–514, <https://doi.org/10.1080/027868299304039>, 1999.
- Zhao, R., Charan, S. M., Kenseth, C. M., Zhang, X., Huang, Y., Charan, S. M., Kenseth, C. M., and Seinfeld, J. H.: Unified Theory of Vapor–Wall Mass Transport in Teflon-Walled Environmental Chambers, *Environ. Sci. Technol.*, 52, 2134,2142, 2018.